J. Fluid Mech. (2003), *vol.* 486, *pp.* 161–188.
DOI: 10.1017/S0022112003004543 Printed in the United Kingdom

An experimental study of wave run-up at a steep beach

By ATLE JENSEN, GEIR K. PEDERSEN AND DEBORAH J. WOOD

Mechanics Division, Department of Mathematics, University of Oslo, PB 1053 Blindern, N-0316 Oslo, Norway

(Received 3 July 2001 and in revised form 19 February 2003)

This paper presents experiments on run-up of strongly nonlinear waves on a beach of 10.54° inclination. Velocity fields are obtained by the PIV (particle image velocimetry) technique. Acceleration measurements are also attempted, but it is difficult to obtain useful results in every case. In addition, free-surface profiles are extracted from digital images and wave resistance probes. The investigation focuses on the dynamics of the early stages of the run-up, when steep fronts evolve in the vicinity of the equilibrium shoreline, but maximum run-up heights are also reported. Measurements on moderately nonlinear waves are compared to results from long-wave theories, including a numerical Boussinesq model and analytic shallow-water results from the literature. In particular the applicability of the long-wave theories is addressed. However, most attention is given to run-up of high incident solitary waves that are on the brink of breaking at the shoreline. In one case a temporarily slightly overturning wave front is found that neither develops into a plunger or displays appreciable spilling. This feature is discussed in view of measured velocity and acceleration patterns and with reference to the dam-break problem. Effects of scaling, as well as viscous damping, are also briefly discussed.

1. Introduction

The present study is particularly motivated by research on tsunamis due to earthquakes and submarine slides. Since 1990 we have not seen any event comparable to the larger historic ones. Nevertheless, during this time thousands of lives have been lost in tsunami disasters, in addition to huge damage to coastal installations and buildings. A complete study of the tsunami phenomenon involves a series of sub-topics of fundamental importance both from a geological and hydrodynamic point of view. However, the ultimate goal is always prediction of the tsunami impact and run-up on shores, breakwaters and harbour installations. Run-up of waves has been an important theme in hydrodynamic wave theory for many decades. In addition to tsunamis the topic concerns a number of other applications, for instance coastal erosion and sedimentation by swells, construction of absorbing beaches in laboratory wave tanks and coastal disintegration of internal waves on the pycnocline.

Theoretical treatment of run-up has traditionally been based on nonlinear shallow-water theory. On plane slopes some analytical solutions have been found for both non-breaking waves (Carrier & Greenspan 1958), and bores (Keller, Levine & Whitham 1960; Shen & Meyer 1963; Meyer & Taylor 1972). The analytical solutions have been developed further by Synolakis (1987) and others. In numerical computations

on an Eulerian grid, points must be dynamically included or excluded from the computational (wetted) domain according to the motion of the shoreline, as reported by, for instance, Hibberd & Peregrine (1979), Flather & Heaps (1975), Kowalik & Murty (1993) and Titov & Synolakis (1998). An alternative is the use of Lagrangian coordinates as is found in, for instance, Pedersen & Gjevik (1983) and Zelt & Raichlen (1990). Crude bore models may be included in long-wave models as jumps, that may be sustained and kept sharp by particular techniques. Synolakis & Skjelbreia (1993) attempts a complete description of shoaling of solitary waves, both post and pre breaking, where various theoretical and experimental results from the literature are employed.

Recent applications of more general models for shoaling and run-up mainly fall into two categories: full potential theory represented as integral equations and Navier–Stokes solvers with volume of fluid (VOF) techniques for the free surface. Important publications based on higher-order boundary integral methods are Grilli & Svendsen (1990) and Grilli, Svendsen & Subramanya (1997) that emphasize breaking criteria and characteristics during run-up and therefore are of particular significance in the present context. Run-up computations based on Navier–Stokes equations are reported by Lin, Chang & Liu (1999), Guignard *et al.* (2001) and others.

Quite a number of experimental investigations on run-up have been reported. Traditionally surface elevations have been measured by wave gauges or the maximum run-up height has been observed visually. Some of the older work is surveyed in Meyer & Taylor (1972), while more recent results for solitary waves are given in Synolakis (1987). Employing digital images and a special optical run-up wave gauge, Li & Raichlen (2001) report surface measurements for solitary waves on a 1:2.08 slope and compare with analytical predictions. Swash zone dynamics is important with respect to sedimentation and beach erosion; see recent reviews by Longo, Petti & Losada (2002) and Elfrink & Baldock (2002). Field measurements involving pressure sensors, current meters, FOBS (fiber-optic optical backscatter sensor) and video tracing of the shoreline were carried out by Puleo *et al.* (2000). Foote & Horn (1999) used video images for surface capturing in the swash zone and observed significant discrepancies from traditional wave probe data. Petti & Longo (2001) employed laser-Doppler velocimetry (LDV) for velocity measurements at selected vertical sections of the swash zone, while wave gauges and cameras were used for surface measurements.

The accurate measurement of velocities within a wave is complicated. However, due to improved technology in the last few decades several methods have been developed that have accomplished this with increasing success. Nadoaka, Hino & Koyano (1989) used a fibre-optic laser-Doppler anemometer (LDA) to study the turbulent flow field under a breaking wave on a 1:20 slope. Ting & Kirby (1995, 1996) employed LDA and wave gauges for a strong plunging and a spilling breaker respectively, on a 1 in 35 slope. They obtained good descriptions of the structure of the turbulence in both types of waves.

Using the newer method of particle image velocimetry (PIV) the full velocity field can be obtained. PIV can still not be used in aerated regions, but, applied with care, the method can be successful in capturing velocities in some other difficult situations such as in the crest of a broken wave (see for example Craig & Thieke 1996). Chang & Liu (1999) present an experimental study using PIV to investigate turbulence in a spilling breaker. They examined the number of repetitions required for obtaining good representations of averaged quantities and concluded that 16 seemed appropriate.

There are also a few studies in the literature on the measurement of accelerations. The measurement of accelerations is difficult because it involves the subtraction of

two velocity fields, at slightly different times, both of which are subject to random noise. Due to the small difference between the velocity fields, the relative error is then dramatically increased. Chang & Liu (1998) in a brief paper give some estimates of accelerations in a overturning jet. Jakobsen, Dewhirst & Greated (1997) describe the techniques for measuring accelerations with PIV and give some analysis on the errors which occur when using this technique. They claim to be able to measure accelerations to within 3–7%. Jensen *et al.* (2001) use a two-camera system for measuring accelerations in Stokes waves. The measurements of accelerations in short-crested waves gave the best results with relative standard deviations down to 2%.

While PIV and LDA experiments on surf zone dynamics has been the subject of a series of papers there has been less work on the detailed velocity distributions for a wave running up a beach. Lin, Chang & Liu (1999) used the volume-of-fluid model (VOF) described in Lin & Liu (1998*a*, *b*) to examine solitary waves running up and down a beach. They compared the computations with PIV experiments for a rather long non-breaking wave on a steep slope of 30°, and found good agreement. Breaking waves on a much milder slope (2.88°) were also computed, but were compared only to the surface measurements of Synolakis (1987), again with good agreement.

Until now, there have been no experimental investigations on the detailed distribution of velocity and acceleration in the run-up of steep waves and breaking waves. In the present article we focus on PIV investigations of the early stages in the run-up of nearly breaking waves. This is an important step toward a more complete understanding of wave run-up. In particular, we believe that run-up of waves bordering on breaking may have important features in common with run-up of bores. The run-up measurements are compared to computations from a Boussinesq-type model, which is fully nonlinear, but does not include higher-order dispersion terms. The main intention behind the comparison is to check the measurements, while emphasis is also put on the applicability of this kind of long-wave model to run-up of steep waves. Some other aspects are pursued in a related paper (Wood, Pedersen & Jensen 2003) where an industrial Navier–Stokes solver is employed. The computations were hampered by a spurious boundary layer at the surface and the steepness of wave fronts during run-up was under-predicted. Nevertheless, reasonable overall agreement with experiments reported herein was achieved for the surface elevation and the velocities.

2. Motivation and basics

2.1. *Experimental set-up and techniques*

The experiments were performed in a wave tank at the Hydrodynamic Laboratory, Department of Mathematics, University of Oslo. The wave tank is 1 m high, 0.5 m wide and is constructed with deviations in the depth and width less of than 0.5 mm. At one end of the tank waves were generated by a hydraulic piston attached to a vertical paddle. A definition sketch of the wave tank and the beach is given in figure 1. The majority of the experiments were carried out with an equilibrium depth, h, equal to 20 cm, while a selection of the experiments were also performed at half-scale. Unless otherwise noted the full scale experiments are reported. In the run-up experiments a rather steep beach, with an inclination $\theta = 10.54°$, is located at a distance $L = 3.705$ m from the initial position of the wave maker. The beach is made of Perspex, which expands a little due to water absorption and becomes slightly bent. Even though the resulting deformation of the beach is small (less than 1 mm),

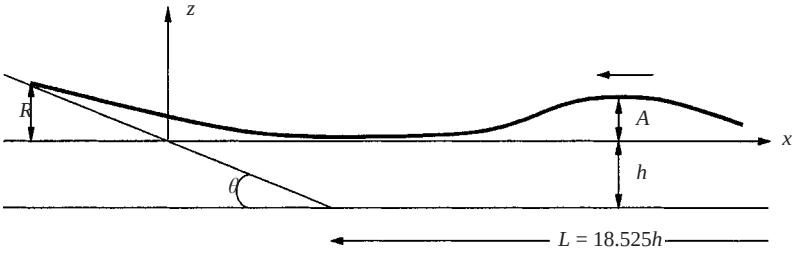

FIGURE 1. Definition sketch of the wave tank.

observable three-dimensionalities near maximum run-up are produced. The slope angle is slightly below the limiting angle of 12.5°, above which no incident solitary wave breaks during run-up, according to Grilli, Svendsen & Subramanya (1997) (see § 2.4).

In the PIV measurements a light sheet was created by a continuous wave (CW) laser and a scanning system. The laser beam was modulated with an acousto-optic modulator which selects two or more pulses for PIV recordings. Highly-sensitive CCD cameras with a resolution of 1280×1024 pixels and 12-bit digital outputs were used for image acquisition. The triggering has a variability of less than the scanning period of the PIV system, set between 1 and 12 ms in the experiments. This limits the repeatability. In all experiments an interrogation window of 64×64 pixels with an overlap of 50% was used. The post-processing procedure and the PIV system are described in more detail by Jensen *et al.* (2001). Conifer pollen was added to the flow as seeding particles. The presence of the organic pollen led to growth of bacteria and algae that increased the opacity of the water, which had to be changed regularly. Hence, in a few measurements in constant depth we switched to 50 μm polyamid particles. No significant differences between the polyamid and the pollen measurements were observed.

Many of the measurements are made in fluid regions above the equilibrium water level and are calibrated according to the sheet being viewed through water. Then, for instance, when the water level is low the surface may be viewed nearly horizontally, or even slightly from above. Consequently, the region near the surface is distorted due to refraction and reflection effects at the free surface. Hence, in some images there was some loss of information near the free surface of the fluid. Naturally, refraction effects at the tank sidewall lead to nonlinearities in the mapping between physical coordinates and the image frame that are not taken into account by the PIV software. However, since we employ small fields of view and the cameras were aligned nearly perpendicular to the tank sidewall these errors were negligible.

During run-up PIV was employed with five fields of view (FOVs) that were chosen according to the characteristics of the different waves and the wish to identify the physical mechanisms in the first stage of the run-up (table 1). The quality of each experiment is carefully checked with respect to the correlation between subsequent images, which occasionally becomes too low. This may be due to inhomogeneous seeding of particles and optical effects that may be linked to pollution of the sidewall of the tank. A sufficient number of repetitions are made to yield a minimum of three measurements that are valid in the interior of the fluid. While this is adequate for a general assessment of repeatability, the typical number of realizations (3–6) is far too small for any rigid statistical analysis of the experimental data. Nevertheless, the

FOV	x-span (cm)	y-span (cm)	Cases (and times)
(i)	$-15.7 < x < 1.2$	$0.9 < y < 14.5$	IV (3.1, 3.12)
(ii)	$-5.5 < x < 6.1$	$0.5 < y < 9.7$	I (4.4), II (3.04), III (3.47), IV (3.05)
(iii)	$-19.5 < x < -7.50$	$3.1 < y < 12.6$	II (3.16), III (3.7), IV (3.14)
(iv)	$1 < x < 22.8$	$-10.6 < y < 6.9$	I (4.55, 4.8. 5.05)
(v)	$-6.9 < x < 6.1$	$-0.15 < y < 9.9$ ($h = 0.1$ m)	III (2.51, 2.62), IV (2.12, 2.18)

TABLE 1. FOVs in cm and trigger times in s.

outcome of the standard deviation formula may yield a fair idea of the quality of the measurements and we refer to it as a scatter measure.

In addition to the velocity measurements by PIV, wave heights were measured by resistance wave probes at two selected locations. The digital images from the PIV system were also used to estimate the free-surface location with a bitmap viewer. Due to optical effects and the high exposure time needed to capture the small pollen particles the digitized surfaces are generally less reliable than the PIV velocities.

2.2. *Accelerations*

Accelerations are much harder to obtain from the PIV technique than velocities. In highly controlled experiments Jensen *et al.* (2001) were able to extract accurate local accelerations ($\partial \boldsymbol{v}/\partial t$) for Stokes waves. Herein we need material accelerations, which imply that spatial gradients must also be accounted for. In spite of the good accuracy and a high degree of repeatability in our PIV measurement, there are still small errors, with rapid spatial and temporal fluctuations, that render extraction of gradients and accelerations difficult. This problem is aggravated since the noise in our run-up experiments is scaled by the large and dominant onshore translation (see § 4), while the velocity gradients are relatively weak. Hence, we have succeeded only for the cases with the largest accelerations compared to the noise level of the velocity fields.

The first step toward determination of gradients is smoothing. Some smoothing, within the interrogation domain, is inherent in the PIV algorithm (see for example Raffel, Willert & Kompenhans 1998). To the resulting PIV velocities we apply the standard symmetric three point smoothing scheme in the interior and the corresponding asymmetric scheme on the boundary. The procedure is generally repeated 2–4 times. The accelerations were computed in two ways from the subsequent velocity fields $\boldsymbol{v}(x, y, t)$ and $\boldsymbol{v}(x, y, t + \Delta t)$. First, finite differences can be applied to calculate all derivatives needed to evaluate the material derivative of the acceleration $\boldsymbol{a} = \partial \boldsymbol{v}/\partial t + \boldsymbol{v} \cdot \nabla \boldsymbol{v}$. However, the results presented herein are obtained by tracing imaginary fluid particles over the time span Δt. Denoting the position and velocity of a particle at t by $\boldsymbol{r}_1$ and $\boldsymbol{v}_1$, respectively, we employ a mid-point integration of position with time to obtain the implicit expression

$$\boldsymbol{v}(x_2, y_2, t + \Delta t) = \boldsymbol{v}_2, \quad \boldsymbol{r}_2 = \boldsymbol{r}_1 + \frac{\Delta t}{2}(\boldsymbol{v}_1 + \boldsymbol{v}_2), \tag{2.1}$$

where $\boldsymbol{r}_2 \equiv (x_2, y_2)$ and $\boldsymbol{v}_2$ are the position and velocity at time $t + \Delta t$. Velocities at locations not coinciding with grid points are generally found by bilinear interpolation, or by linear interpolation within triangles close to the fluid margin. Equation (2.1) is solved by a simple iterative technique, where new $\boldsymbol{r}_2$ and new $\boldsymbol{v}_2$ are computed alternately. Generally, two iterations suffice. Finally the acceleration is calculated by

the difference

$$\boldsymbol{a} = \frac{1}{\Delta t}(\boldsymbol{v}_2 - \boldsymbol{v}_1). \tag{2.2}$$

Naturally, this approximates most closely the value at position $\boldsymbol{r} = \frac{1}{2}(\boldsymbol{r}_1 + \boldsymbol{r}_2)$ and time $t + \frac{1}{2}\Delta t$. However, the error by assigning it to the coordinates $\boldsymbol{r}_1$ and t is small compared to the errors inherited and amplified from the velocity fields.

2.3. *The Boussinesq-type model*

The experiments are compared to solutions of a set of Lagrangian Boussinesq-type equations similar to those described in Pedersen & Gjevik (1983, referred to herein as PG). In traditional Boussinesq-type equations the dispersion term is linearized. In PG only the dispersion terms involving products of velocities were omitted, while nonlinearities in displacements were retained. However, in our detailed study on steep waves in the early stages of run-up it seems appropriate to avoid any kind of linearization to eliminate this as a potential error source.

Following the usual convention of using a typical depth h_0 and a wavelength L as vertical and horizontal length scales, respectively, and $(gh_0)^{1/2}$ as velocity scale, we introduce dimensionless variables. Note that these are employed only in the present subsection and at the end of the Appendix. The long-wave parameter now becomes $\beta \equiv h_0^2/L^2$. We seek equations with relative error of order β^2, while all terms of order β are kept, regardless of the degree of nonlinearity. By some tedious, but straightforward, algebra we derive such an equation from intermediate results in PG. Omitting a few details that are irrelevant in the present context, their fully nonlinear momentum equation can be expressed as

$$\frac{\mathrm{D}\overline{u}}{\mathrm{D}t} = -\frac{\partial \eta}{\partial x} + \beta \frac{\partial}{\partial x}\left(\overline{E} - E|_{y=\eta}\right), \tag{2.3}$$

where $\overline{()}$ indicates vertical averaging, η is the surface elevation and $(\mathrm{D}/\mathrm{D}t) \equiv (\partial/\partial t) + \overline{u}(\partial/\partial x)$ is a material derivative. The quantity E may be expressed as

$$E \equiv \frac{\mathrm{D}\hat{\phi}}{\mathrm{D}t} + \frac{1}{2}\left(\frac{\partial \hat{\phi}}{\partial x}\right)^2, \quad \hat{\phi} = \frac{1}{2H}\frac{\mathrm{D}H}{\mathrm{D}t}y^2 + \left(\frac{\mathrm{D}\eta}{\mathrm{D}t} - \frac{1}{H}\frac{\mathrm{D}H}{\mathrm{D}t}\eta\right)y, \tag{2.4}$$

where $H \equiv h + \eta$ is the total water depth and $\hat{\phi}$ is the part of the velocity potential that corresponds to the vertical velocity. Expanding the rightmost term of (2.3), correcting a minor typing error in (2.3) of PG, and including the equation of continuity we arrive at the set

$$\frac{\mathrm{D}H}{\mathrm{D}t} = -H\frac{\partial \overline{u}}{\partial x}, \tag{2.5a}$$

$$\left(1 - \tfrac{1}{2}\beta H h'' - \beta h' \frac{\partial}{\partial x}\right)\frac{\mathrm{D}\overline{u}}{\mathrm{D}t} = -\frac{\partial \eta}{\partial x} - \frac{\beta}{3}\left[H\frac{\partial}{\partial x}\left(\frac{\mathrm{D}^2 H}{\mathrm{D}t^2}\right) + 2\frac{\partial H}{\partial x}\frac{\mathrm{D}^2 H}{\mathrm{D}t^2}\right] + \beta\left[\frac{h'}{H}\left(\frac{\mathrm{D}H}{\mathrm{D}t}\right)^2 - h''\overline{u}\frac{\mathrm{D}H}{\mathrm{D}t} + \left(\frac{\partial \eta}{\partial x}h'' + \frac{1}{2}Hh'''\right)u^2\right], \tag{2.5b}$$

where h' is the x-derivative of the equilibrium depth. In comparison to the formulation of PG there are two groups of new terms, that both vanish in constant depth. One group is collected in the last line of the momentum equation (2.5*b*). It is noteworthy

that only one of these terms contributes on a plane slope, and their effect is generally very small. Slightly more important is the term, rightmost within the parentheses, on the left hand-side of the momentum equation. This is the only term of order β that is non-vanishing at the shoreline on a plane slope, yielding a shoreline acceleration $\mathrm{D}\overline{u}/\mathrm{D}t = -\partial\eta/\partial x/(1 - \beta h'\partial\eta/\partial x)$. Hence, there is a singularity in the shoreline acceleration when the fluid surface is perpendicular to the beach, while the PG formulation remains regular until the surface becomes vertical. This imply differences concerning breaking, but the singularities are in any case beyond the validity range of the equations. For a solitary wave with $A/h = 0.34$, we find that the new term introduce a 1%, say, change in the run-up phase that mainly corresponds to a time delay (about 0.002 s for $h = 20$ cm). The effect on the maximum run-up height is much smaller.

Due to the higher-order derivatives of h in the momentum equation we need third-order continuous derivatives of the depth function. Hence, the angle between the beach and bottom is replaced by a sixth-order spline extending some fraction of the slope length. Tests indicate that this deviation from the laboratory geometry may give rise to relative errors of order 10^{-3}.

As in PG we define an averaged Lagrangian coordinate a according to

$$\frac{\mathrm{D}a}{\mathrm{D}t} = 0.$$

Recognizing the material derivative as the partial Lagrangian temporal derivative we may integrate the continuity equation (2.5*a*) to obtain

$$H\frac{\partial x}{\partial a} = H_0,$$

where H_0 is the initial height of the fluid column. We note that this equation explicitly expresses mass conservation in the column. The full Lagrangian version of (2.5) is now easily obtained by making the replacements

$$\frac{\mathrm{D}}{\mathrm{D}t} \to \frac{\partial}{\partial t}, \quad \frac{\partial}{\partial x} \to \frac{H}{H_0}\frac{\partial}{\partial a}.$$

The advantage of the Lagrangian formulation is that both the shoreline and paddle positions are associated with fixed values of a. At these locations we invoke the boundary condition $H = 0$ and the measured paddle motion, respectively.

Our numerical method employs a staggered time discretization (x, H and u at adjacent temporal positions), whereas PG used a Crank–Nicholson scheme. We then obtain improved dispersion properties at the cost of unconditional stability, while an iteration procedure now is needed to incorporate all nonlinearities with second-order accuracy. Otherwise the methods are very similar and the numerical representation of the additional nonlinear dispersion terms is rather straightforward. Hence, apart from noting that no filtering of any kind is applied and that linear wave modes in constant depth are neutrally stable (no damping inherent in the model), we omit further details on the numerical technique. For the nonlinear shallow-water equations a similar Lagrangian model has been presented and tested for three-dimensional problems, as well as propagation and run-up of bores (Johnsgard & Pedersen 1997; Johnsgard 1999).

When the Lagrangian counterpart of (2.5) has been solved numerically, the requirements of zero divergence and rotation may be used to restore the vertical

variations in the velocity fields according to

$$\left.\begin{aligned} v(x,y,t) &= \left(\frac{\mathrm{D}\eta}{\mathrm{D}t} + \frac{\partial \overline{u}}{\partial x}(\eta - y) + O(\beta)\right), \\ u(x,y,t) &= \overline{u} + \beta\left(A_1\left(y + \tfrac{1}{2}H\right) + A_2\left(y^2 - \tfrac{1}{3}H^2\right)\right) + O(\beta^2), \\ A_1 &= \frac{\partial}{\partial x}\left(\frac{\mathrm{D}\eta}{\mathrm{D}t} + \eta\frac{\partial \overline{u}}{\partial x}\right), \quad A_2 = -\frac{1}{2}\frac{\partial^2 \overline{u}}{\partial x^2}. \end{aligned}\right\} \tag{2.6}$$

To evaluate these expressions at the appropriate spatial and temporal position we apply an extra set of interpolation and differencing to the numerical solution. However, grid refinement tests ensure that the total discretization errors are negligible, apart from in the close vicinity of the instantaneous shoreline.

2.4. *The run-up phenomenon*

Following, in part, Grilli, Svendsen & Subramanya (1997), we may define four regimes for run-up of solitary waves on beaches. Generally, on going down the list, as given below, the amplitude increases or the beach inclination decreases, even though not all the regimes may be observed for a given beach inclination.

(*a*) A smooth and gentle run-up where the surface gradient never becomes vertical. The steeper waves in this regime break during backwash.

(*b*) The wave front becomes vertical, or nearly vertical, when the wave reaches the equilibrium shoreline. The steep front may propagate some distance up-beach, but it never forms a plunger and is transformed into a smooth thin wedge of fluid that climbs the beach. The range of this intermediate regime may be appreciable. For instance, for run-up on a 1:8 slope beach Grilli, Svendsen & Subramanya (1997) report that solitary waves with amplitude/depth ratios ranging between 0.25 and some upper limit above 0.4 belong here. In Grilli, Svendsen & Subramanya (1997) the denotation surging breaker is used for the steep fronts in this intermediate regime. However, we do not employ this herein.

(*c*) The incident wave produces a plunger in the vicinity of the equilibrium shoreline. In some cases a 'splash-up' is observed when the plunger hits the beach.

(*d*) Breaking occur at a finite distance from the shore and a fully developed bore is produced. At the shoreline the bore vanishes and a thin tongue of fluid flows up the beach, as for case (*b*).

Naturally, there are other ways of defining regimes and the boundaries between the regimes may be hard to determine accurately. However, there are a few breaking criteria available in the literature, among which we mention two. Based on analytic solutions where hydrostatic, nonlinear equations at the slope are patched to a linear hydrostatic regime in the adjacent flat bottom region, Synolakis (1987) arrived at

$$\frac{A}{h} = 0.818(\tan\theta)^{10/9}. \tag{2.7}$$

Grilli, Svendsen & Subramanya (1997) reports a breaking criterion for solitary waves based on least-squares fitting of computational results obtained from a boundary element method for full potential flow. Expressed in our notation the criterion reads

$$\frac{A_*}{h} = C_* \tan^2\theta, \tag{2.8}$$

where $C_* = C_b = 16.9$ and $C_* = C_c = 25.7$ define the lower limits of regimes (*b*) and (*c*), respectively. Inserting our slope inclination, $\theta = 10.54^\circ$, we find $A/h = 0.126$

and $A_b/h = 0.585$ from (2.7) and (2.8) respectively, while A_c exceeds the maximum solitary wave amplitude of approximately $0.83h$. That (2.7) yields a lower value is to be expected since omission of dispersive terms leads to over-prediction of steepening during shoaling. Moreover, the large discrepancy indicates that hydrostatic theory is inappropriate for the high (and short) incident solitary waves that are close to breaking for $\theta = 10.54°$.

Herein we are primarily concerned with cases (*a*) and (*b*). However, it is useful to give a brief discussion of regime (*d*), run-up of bores, which is particularly important with respect to tsunami applications. Within the scope of nonlinear shallow-water theory, with bores represented as discontinuities, there is a fairly complete analytical tradition in the literature, reviewed by Meyer & Taylor (1972). The incident bore evolves smoothly during shoaling, but vanishes, or rather collapses, very rapidly at the equilibrium shoreline. Run-up then occur as a thin tongue, where gravity dominates the pressure gradient parallel to the beach. A crude conception of the run-up itself, as long as frictional effects are neglected, may then be a set of independent fluid particles following parabolic trajectories in time. The maximum run-up height of each particle then depends on its velocity when 'released' close to the shoreline, which in turn is defined by the characteristics of the bore collapse. For physical bores this velocity may be influenced by details of the bore structure, as well as the width compared to amplitude. Concerning run-up predictions, this may make questionable the applicability of the crude bore models in shallow-water theory, where the bore is represented as discontinuity with no specific width or structure. The run-up of regime (*b*) waves, as well as steeper waves of regime (*a*), follow a pattern similar to that of incident bores. A steep wave propagates to, or somewhat beyond, the equilibrium shoreline where it collapses and is transformed rapidly to a thin jet that again is dominated by gravity (see figure 3*b* below). Hence, the study of nearly breaking waves may be a good starting point for run-up investigations and the transformation of the steep front should be scrutinized.

Maximum run-up heights are not the key issue of the present work, but observed values are reported and compared to theory. From Synolakis (1987) we have the simple asymptotic ($A/h \gg 8.3\tan^2\theta$) expression

$$\frac{R}{H} = 2.831\sqrt{\cot\theta}\left(\frac{A}{H}\right)^{5/4}, \tag{2.9}$$

which is based on the same theory as (2.7). The formula (2.9) agrees well with computations of maximum solitary wave run-up from our Boussinesq model for small A/h and θ, while it yields higher values for larger A/h. This is probably because the nonlinear shallow-water theory yields too much steepening during shoaling, which in turn produces too high a run-up. Our inclination angle, $\theta = 10.54°$, is a little large for (2.9), but the formula gives the same results as the Boussinesq model for A/h around 0.08. However, an important observation is that both the model and (2.9) always give run-up amplification factors, R/A, that grow with A/h, though at a decreasing rate for increasing A/h.

2.5. *Wave generation*

With regard to tsunami applications the most appropriate choice would be incident waves with a long elevation following a steep front, or a long trough terminated by a steep gradient, in either case reflecting common characteristics of tsunamis in coastal waters. However, limitations on the wave paddle motion rendered the creation of such waves with appreciable amplitudes impossible and solitary wave-like pulses were

employed instead. Within the dispersive long-wave regime the vertical distribution of horizontal velocity is nearly uniform, which implies that a vertical paddle in principle may produce any wave profile accurately, if the Lagrangian trajectories are computed. Details concerning the generation of solitary waves in this way (Gorings method) as well other wave profiles are given in Synolakis (1990). For high-amplitude solitary waves, on the other hand, dispersive long-wave theory is not adequate. Utilizing the fully nonlinear and dispersive solution of Tanaka (1986) we have obtained vertically averaged trajectories that have been employed in a generalized Gorings method. Even though the paddle still fails to reproduce the correct velocity profile, in this manner we are able to produce very close approximations to solitary waves with amplitudes up to half the depth. This is the highest wave we attempt to create, due to the limitations on the wave paddle. However, to approach the breaking limit this amplitude is insufficient and we have to resort to other, and cruder, generation techniques. Hence, we abandon Gorings method and invoke a strong impulsive motion of the paddle that conveys more energy to the water and thus produces higher waves. Of course, these are not perfect solitary waves at the outset, but for the higher amplitudes, at least, nearly solitary wave-like shapes evolve within a couple of metres in the tank.

Experiments are reported for four different incident waves. Their properties may be summarized as follows

I: $A/h = 0.12$. A gentle, long wave, well within regime (a) as described in § 2.4, which should be described well by dispersive long-wave theory and is the only one that displays significant deviations from a solitary wave shape. This wave serves mainly as a check on the experimental procedure and numerical model.

II: $A/h = 0.53$. A steep wave with amplitude just below the limit to class (b) according to (2.8). This case is mainly useful for comparison case IV below.

III: $A/h = 0.335$. A moderately high incident wave (regime a) close to a solitary wave. It should be described rather well by a Boussinesq-type model in finite depth. At the beach, on the other hand, it becomes rather steep and challenging for long-wave theory.

IV: $A/h = 0.665$. This wave is close to the steepest one we were able to produce with no breaking from generation and past maximum run-up and is well within regime (b) according to (2.8). Emphasis is put on velocity and acceleration distributions when the wave front is at its steepest.

Details on the measurement of the amplitudes are given in § 3.1.

The paddle motion is governed by a input signal with the voltage specified by a fifth-order polynomial that ensures continuous second derivatives. For gentle paddle motion the response of the paddle is nearly perfect, in the sense that its position is always proportional to the input voltage. However, this is not case for the rapid paddle motion employed in the present investigation. Hence, in every experiment the actual paddle position is measured, by means of a 1 kHz magnetic digital measurement system (Jensen & Grue 2002). These measurements are used as input for the Boussinesq model. The duration and total displacement for cases I to IV are given in table 2, while displacements as a function of time are shown in figure 2. For cases I, II and III the total paddle displacement is identical, while different amplitudes and wavelength are produced by changing the speed of the paddle. The displacement for case IV is the largest possible, due to limitations on the wave maker, and to produce the high amplitudes of cases II and IV the paddle motion must be significantly quicker than the particle motion in the corresponding solitary waves.

With a smaller depth, $h = 10$ cm, we wish to reproduce the non-dimensional paddle motion from figure 2. Save for viscous and capillary effects, we should then obtain a

Case	D_{max} (cm)	T (s)
I	28.69	3.333
II	28.69	0.714
III	28.69	1.429
IV	36.75	1.000

TABLE 2. Paddle parameters: D is displacement and T is period.

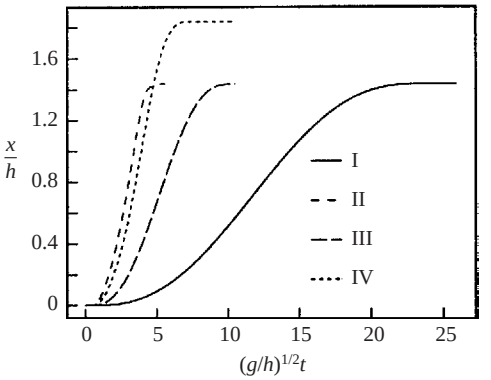

FIGURE 2. Non-dimensional paddle motion for all cases.

wave motion similar to the one for $h = 20$ cm, with all lengths halved and the time scale reduced by a factor $\sqrt{1/2}$. Due to the imperfect, but highly repeatable, response of the wave paddle, this is not obtained simply by scaling the voltage distribution. Instead the correct voltages for $h = 10$ cm are obtained by an iteration procedure where deviations of the measured paddle motion from the desired one, are used to adjust the input voltage.

2.6. *Boussinesq simulations*

For each case the Boussinesq model is run with a series of resolutions, ranging from 80 to 10 000 points covering the whole wave tank. Close convergence is generally obtained for the coarsest of these resolutions. However, small-scale features with slower convergence are observed at the shoreline during the first run-up phase that is characterized by a very steep wave front. The coarsest grids employed for cases II and IV yield smooth run-up. Even though the maximum steepness during run-up still increases with resolution, good convergence is observed otherwise (maximum run-up height etc.). For finer grids the solution passes the singularity (discussion below equation (2.5)) and then rapidly breaks in the sense that $\partial x/\partial a \leqslant 0$. It is tempting to assume that quantities like run-up heights obtained from the coarse grids may still be of significance. However, according to the Appendix this is doubtful since the Boussinesq equations do not reproduce the behaviour of steep wave fronts properly. Also the formulation of PG yields breaking during run-up for cases II and IV and refined grids.

Even for case III there are some small-scale features that becomes resolved only for very fine grid (figure 3*a*), but overall convergence has already been obtained for 160 points.

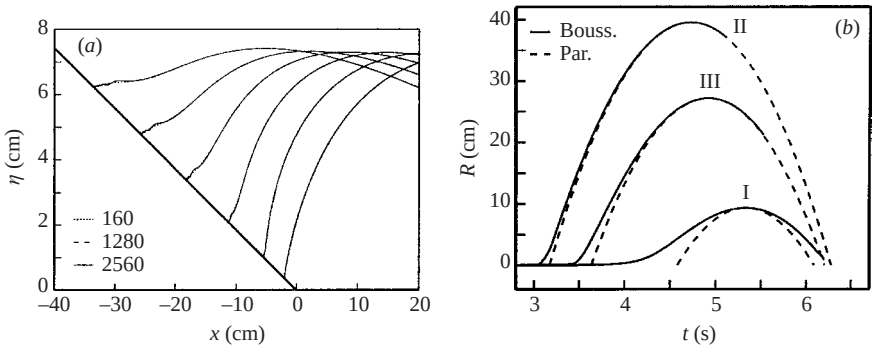

FIGURE 3. (*a*) Progression of run-up front for case III, between $t = 3.46$ s and $t = 3.71$ s, from Boussinesq simulations with 160, 1280 and 2560 grid points. The interval between each surface is 0.0501 s. (*b*) Run-up heights (cm) from the Boussinesq model as function of time (s) for cases I to III. The numerical results are compared to the 'parabola' solution as explained in the text.

As noted in § 2.4 gravity dominates in the run-up tongue for bores. Assuming that this may be the case for steep non-breaking waves also we anticipate that the parabola approximation

$$R \approx R_{\max} - \tfrac{1}{2} g \sin\theta \cos\theta (t - t_m)^2 \tag{2.10}$$

is valid around the time of maximum run-up, t_m. According to figure 3(*a*), this is indeed the case for our Boussinesq simulations, except for the gentle case I. The curve for case II is based on a coarse-grid solution.

3. Propagation in finite depth

3.1. *Incident waves*

To characterize incident waves and verify the PIV procedure a set of PIV and wave gauge measurements were taken in constant depth, either in the absence of, or in front of, the beach. In both cases, reflection from the slope, beach or endwall did not affect the leading crest of the wave markedly.

Comparisons of measured velocities and wave heights are made with solitary waves as obtained by the method of Tanaka (1986) as well as our Boussinesq model, run with the actual paddle motion as boundary input (see § 2.3). For the Tanaka solution Cauchy's theorem was applied to the complex velocity $(u - \mathrm{i}v)$ to obtain the velocities below the free surface.

Time gauge measurements at 3.775 m from the paddle ($h = 20$ cm, no beach), are compared with theory in figure 4. Cases II to IV are close to the solitary wave solution of Tanaka. The long and moderately nonlinear wave of case I has not yet produced a solitary wave at this stage, but is, on the other hand, described well by the Boussinesq model. For cases II and IV the Boussinesq model deviates strongly from measurements, while the deviations are smaller, but still appreciable, for case III. It is noteworthy that the digitized surfaces from images (table 3) yield a slightly lower amplitude for case III, indicating a somewhat reduced error for the Boussinesq model.

In the PIV measurements with $h = 20$ cm the distance from the wave maker to the local origin of the FOV is 3.705 m. Other parameters for the PIV measurements in deep water are listed in table 3, which also summarizes the computed and measured amplitudes.

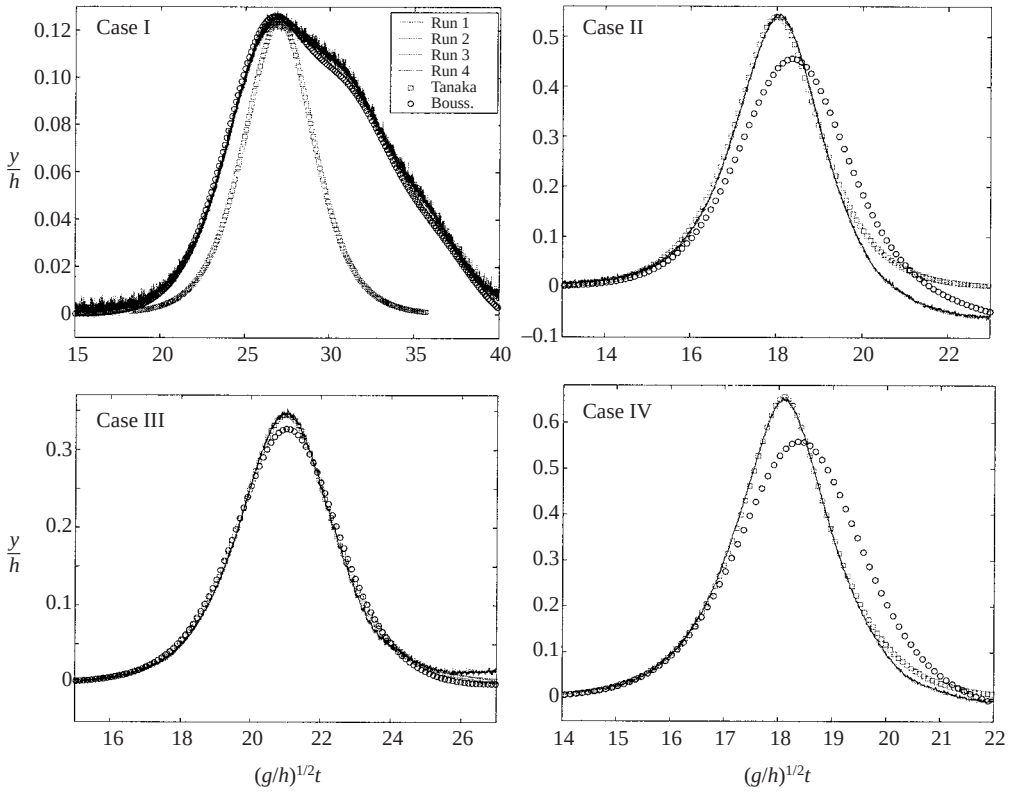

FIGURE 4. Wave elevation in deep water: comparison between theory and measurements.

Case	t_{tr} (s)	Δt_1 (ms)	A (PIV)	A (Bouss.)	Δx (Bouss.)	A (WG)
I	3.85	12	2.4	2.53	—	2.5
II	2.57	6	10.73	9.12	−9.5	10.7
III	2.97	10	6.64	6.54	−3.2	6.9
IV	2.57	4	13.25	11.18	−9.1	13.2

TABLE 3. Amplitudes A (in cm), from PIV images (PIV), Boussinesq simulations (Bouss.) and wave gauges (WG). The phase lag, Δx, is defined as the difference (in cm) between the maximum of the digitized surfaces and the Boussinesq solution at $t = t_{tr}$, which is the trigger time of the PIV measurements. Negative values correspond to delayed simulated waves. The digitized surface of case I has error due to unfavourable camera angle. Hence, the extracted amplitude is uncertain to a few mm. Δt_1 is the time increment between the two images are used in the velocity calculation.

Figure 5 shows the full velocity field (case IV), both for PIV and the Tanaka solitary wave solution. The free surfaces in the digital images are severely over-exposed. Nevertheless, we observe good agreement for the surface, while experiments and theory are almost identical concerning velocities. The scatter between five different runs is generally found to be less than 1%, but larger immediately beneath the free surface. This is to be expected because the noise in the correlation peak increases when the particles cross-correlate with the highly exposed surface. By a combination of PIV and the reflective mode of the free-surface gradient detector (FSGD) technique

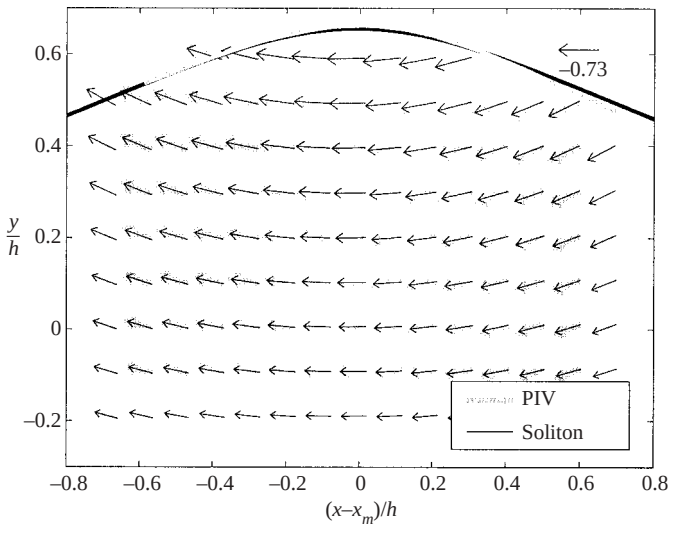

FIGURE 5. Full velocity field ($u/\sqrt{gh}$) with extracted surfaces (case IV), from both experiments and theory. Grey: PIV, black: Tanaka (solitary wave) and $x_m = 5.3$ cm or 3.758 m from the paddle.

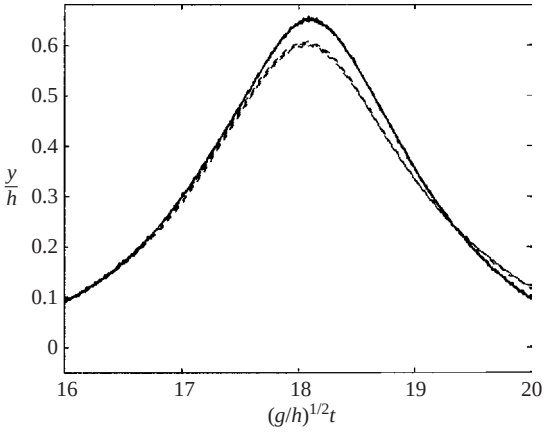

FIGURE 6. Wave gauge measurements for case IV. The solid lines are composed of four runs with $h = 20$ cm, while the dashes respresents three runs with $h = 10$ cm.

it is possible to compute velocity vectors somewhat closer to the surface, see Dabiri & Gharib (2001), but this is not attempted herein.

3.2. *Viscous effects, wave attenuation*

Wave gauge measurements are also performed for $h = 10$ cm. Significant deviations were found for case IV (figure 6). Halving the equilibrium depth causes a reduction in A/h of 0.04. This is probably due to viscous damping, which is more pronounced for shallower water. We have no direct measurements of the amplitude variation along the tank and base the assumption on results from the literature. A theoretical model, based on laminar boundary layers, is found in Keulegan (1948). According to this

model the attenuation of a solitary wave becomes

$$A = A_0 \left\{ 1 + 0.237 \left(\frac{A_0}{h} \right)^{1/4} \left(\frac{\nu c_0}{8h^3} \right)^{1/2} \left[1 + \left(\frac{2h}{b} \right) \right] t \right\}^{-4}, \tag{3.1}$$

where $A_0 = A(t = 0)$, ν is the kinematic viscosity, c_0 is the linear wave speed and b is the width of the tank. The model does not take turbulence or surface effects into account. Shuto (1976) reported the partly empirical formula

$$A = \frac{A_0}{\left(1 + \frac{8}{15} C_1 A_0 x / h^2\right)}, \tag{3.2}$$

where C_1 is a friction coefficient based on measurements and is 0.0227 and 0.0137 for water depth 10 cm and 20 cm, respectively. Equation (3.2) implies a stronger damping than (3.1). In our experiments the wave is not close to a solitary wave all the way from the paddle. Nevertheless, equation (3.2) should give a good indication of damping due to viscous and surface effects. Employing (3.1), with the appropriate parameters for case IV, we obtain a reduction of A/h of 0.007 and 0.011 for $d = 20$ cm and $d = 10$ cm, respectively. The corresponding results for (3.2) are 0.055 and 0.086. In view of the inaccuracies of the surface measurements and the deviations from a perfect solitary wave shape the latter is in good agreement with the amplitude difference from our wave gauge measurements. For case III the scaling effect is smaller relative to experimental errors. In addition the larger relative difference between the amplitude from the images and that from the wave gauge (table 3) casts doubt on the latter. However, the gauge data indicate a reduction in A/h of order 0.01 when h is halved. This is of the same order of magnitude as the prediction by (3.2).

4. Experimental results

We have utilized PIV in several fields of view (FOVs) near the equilibrium shoreline. For illustration the run-up of wave IV, together with the camera set-up, is shown in figure 7.

4.1. *Case I*

In figure 8 we compare surfaces from the experiments with the Boussinesq model for case I. The agreement seems very good for $t = 4.8$ s while discrepancies are apparent for $t = 4.4, 4.55$ s, when the temporal variation of the surface is faster. However, it should be noted that the surface at $t = 4.4$ s is not accurately obtained, due to light refraction effects in the experiments.

A few selected vertical velocity profiles are depicted in figure 9 and compared to profiles that have been reconstructed from the Boussinesq model (see § 2.3). For the horizontal velocities we observe an error, systematic in the sense that the Boussinesq solution seems to be 0.05 ahead, while a conservative estimate of errors (amplitude, equilibrium depth, solitary wave celerity) during propagation in finite depth amounts to 0.02 s. However, if we shift the Boussinesq solution by 0.05 s, both the weak vertical variation and the magnitude agree very closely with the experiments. This is demonstrated in figure 10, where the distribution of vertically averaged velocities in the FOV is compared. For the much smaller normal velocities the scatter range in the experiments is larger in relative terms, and the Boussinesq solution is within this. In general, the overall agreement is as good as can be expected for case I and very good agreement concerning velocities can be obtained by a systematic time shift. However,

FIGURE 7. Run-up of wave IV.

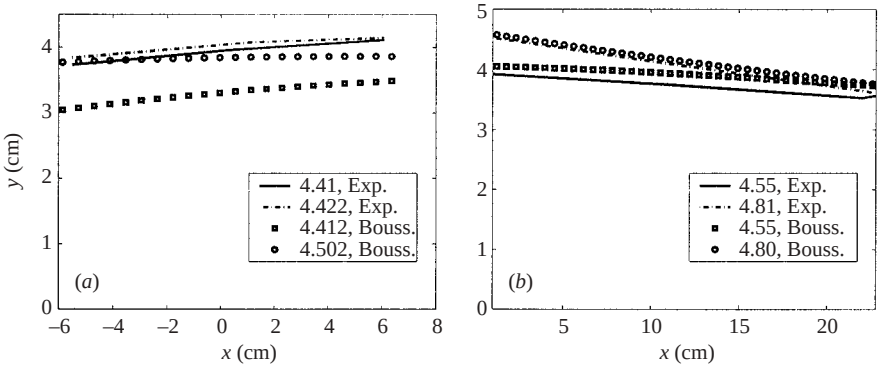

FIGURE 8. Case I: extracted surfaces from the PIV (exp.) images compared to the Boussinesq solution.

simultaneous agreement for velocities and surface cannot be obtained in this manner. Even though the extraction of the free surface is hampered by errors (in particular for $t = 4.4$ s) some of the deviations are likely to be due to the inaccuracy of the Boussinesq equations employed.

4.2. *Case III*

For the steeper wave of case III the errors of the Boussinesq equations are already significant in finite depth (see § 3.1). In an early stage of the run-up figure 11 shows that the deviations for the surfaces are greater than those of case I, but the agreement is still good. This time we are not able to reproduce the horizontal velocities by introducing a consistent time shift in the Boussinesq solution. According to figure 12 we need a positive time shift for $t = 3.47$ s, as for the propagation in constant depth (see § 3.1), whereas a negative shift gives best agreement for $t = 3.7$ s. Inview of the short interval between these two measurements, it seems that the Boussinesq solution,

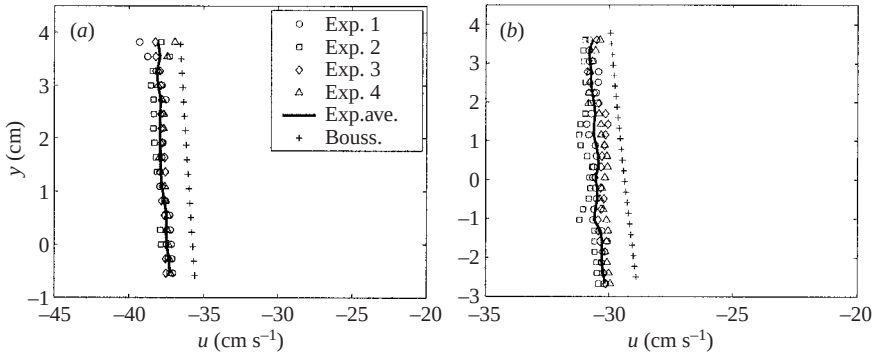

FIGURE 9. Case I, $t_{tr} = 4.55$ s: Velocity profiles of u. (a) $x = 3.5$ cm, (b) $x = 14$ cm.

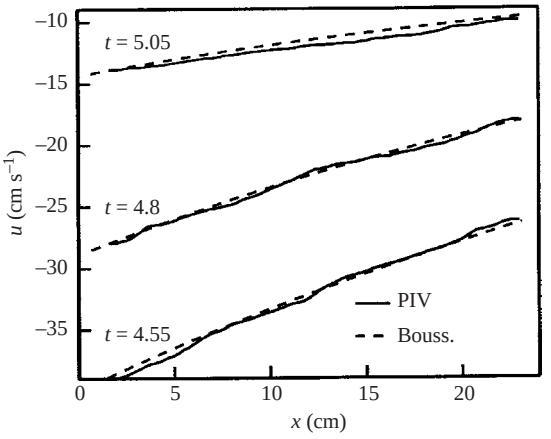

FIGURE 10. Distribution of vertically averaged u along the FOV. The Boussinesq results are consistently shifted by -0.05 s.

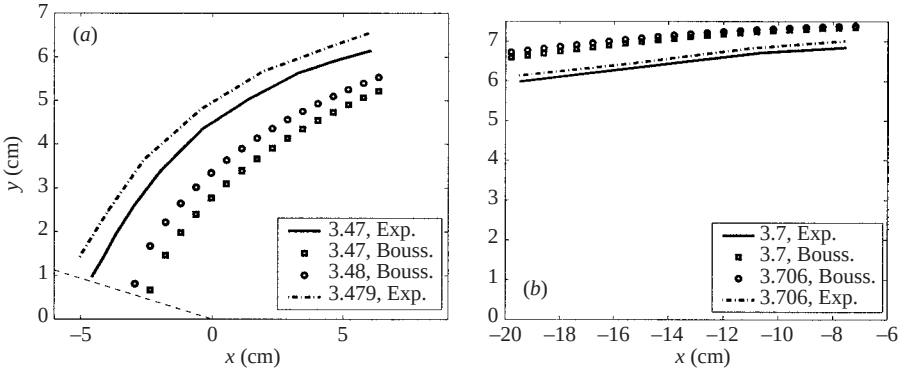

FIGURE 11. Case III: extracted surfaces from the PIV images compared to the Boussinesq solution.

in a sense, evolves much too fast. This can also be inferred from the surfaces in figure 11. According to the computed and measured surfaces at $t = 3.47$ s, the surface gradient of the Boussinesq model is markedly larger than the measured one. We have insufficient data to decide whether over-estimation of the wave front steepness may

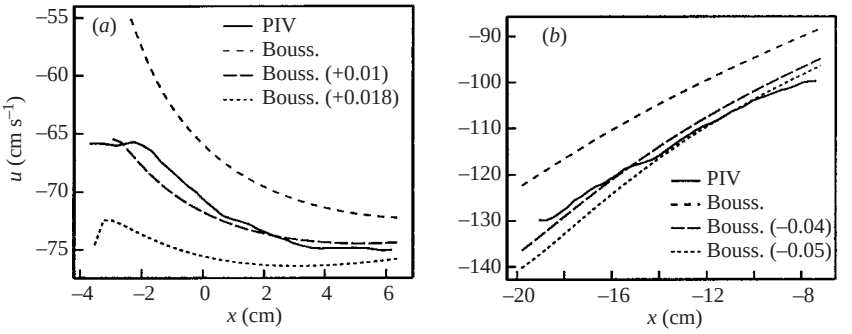

FIGURE 12. Distribution of vertically averaged u along the FOV for case III. (*a*) $t = 3.47$ s, (*b*) $t = 3.7$ s.

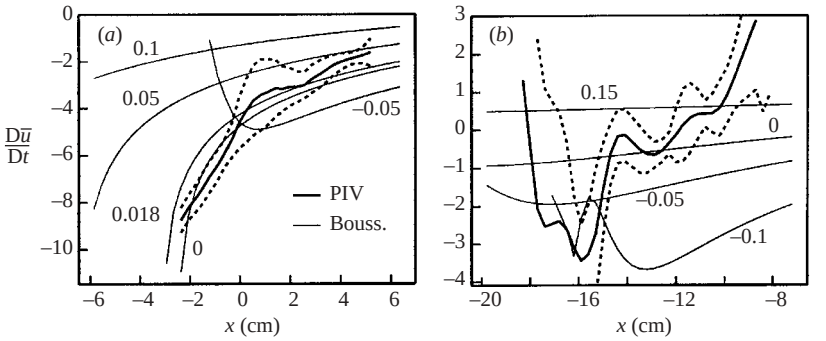

FIGURE 13. Distribution of the vertically averaged, horizontal component of the material acceleration (m s^{-2}) along the FOV for case III. The dashed lines indicate the experimental scatter, while the numbers on the Boussinesq curves are times relative to the PIV time. (*a*) $t = 3.47$ s, (*b*) $t = 3.7$ s.

be a characteristic feature of the Boussinesq model or if the model is mainly out of phase with a delayed occurrence of the maximum surface steepness. Accelerations are obtained from the measurements with limited precision only. However, according to figure 13 there is good agreement with the Boussinesq results for the averaged horizontal accelerations at $t = 3.47$ s, when the magnitude is comparable to g. To some extent the over-representation of dispersion in the Boussinesq model may counterbalance the excess steepness as far as horizontal accelerations are concerned. On the other hand, a significant deviation in the accelerations may be obscured by experimental errors. The much smaller experimental accelerations at $t = 3.7$ s are nearly lost in the noise level. Still, the results at $t = 3.7$ s may indicate important qualitative and quantitative deviations in the Boussinesq solution at this stage. Anyhow, the interval $3.47\,\text{s} < t < 3.7\,\text{s}$ is characterized by rapid variations and a complete change in the nature of the flow. That such errors are pronounced at this stage of the run-up is not surprising since the fluid front is steep and evolves very rapidly, both of which challenge a long-wave expansion. It is not surprising that the Boussinesq model becomes rather inadequate at this stage, but to assess its performance in a more complete way, we would need measurements at more times, in more FOVs and, preferably, more information on the shoaling phase.

It is tempting to assume that the investigated time for case I corresponds to $t = 3.7$ s, rather than $t = 3.47$ s, for case III, since the wave is well past the equilibrium shoreline.

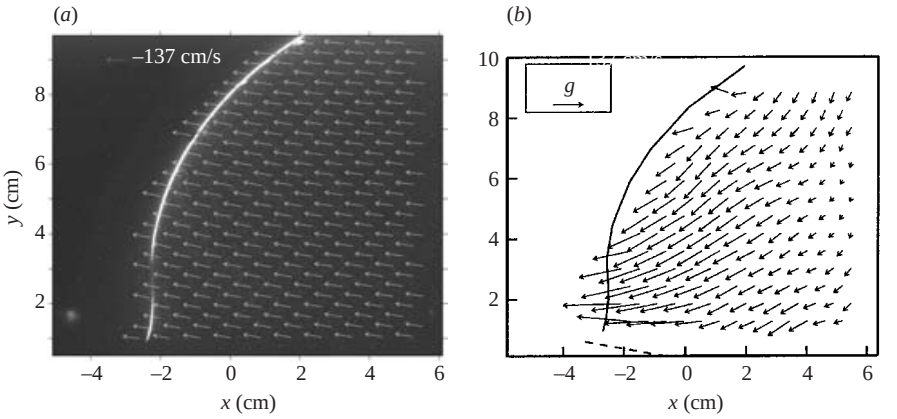

FIGURE 14. Measured velocities and accelerations for case IV at $t = 3.05$. (*a*) Vector plot on a PIV image. (*b*) Particle accelerations.

The too fast evolution of the Boussinesq velocities for case I may thus be due to errors in the non-hydrostatic pressure of the same kind as for case III, but of much smaller magnitude.

4.3. *The steep waves: cases IV and II*

Postponing the description of case II, we now turn to the highest of our waves and investigate the run-up of case IV waves in some detail. During propagation in finite depth the incident wave has maximum horizontal velocity near the peak, while the largest horizontal accelerations are found in the wave front, not far from the position of maximum surface gradient. In shoaling water the front steepens and become shorter, but with the same qualitative distributions of horizontal velocity and accelerations. However, when the wave reaches the equilibrium shoreline the nature of the motion changes from being wave-like to become a material fluid body ascending the beach. An image, overlaid with the velocity field from PIV, for $t = 3.05$ s is shown in figure 14(*a*). The wave has just started to climb the beach and we can see an almost vertical front of the wave. At this stage the dominant feature of the flow is a large, nearly uniform velocity parallel to the beach slope. However, there are small spatial variations in the velocity field that are important because they determine the evolution (deformation) of the shape of the run-up front. Hence, we may regard the velocity field as a uniform translation, on which there is superimposed a 'deforming' velocity field, $\boldsymbol{v}_d$, of smaller magnitude, that contains all the gradients:

$$\boldsymbol{v}_d(x, y, t) = \boldsymbol{v}(x, y, t) - u_0(t)(\boldsymbol{i} - \tan\theta\, \boldsymbol{j}). \tag{4.1}$$

We seek to identify and discuss $\boldsymbol{v}_d$ from the PIV measurements. The translation velocity u_0 is slightly ambiguous, but the actual choice is not crucial as long as the residual field provides a clear pattern. A more grave problem is that the errors in the measurements of the large velocities (up to $1.5\,\mathrm{m\,s^{-1}}$) are augmented, in relative terms, when retained in the much smaller residual field (typically 0.1–$0.2\,\mathrm{m\,s^{-1}}$). For $t = 3.05$ s, we have displayed $\boldsymbol{v}_d$ in figure 15. Even though the errors are noticeable, the repeatability is still rather good with a scatter that is generally less than $1\,\mathrm{cm\,s^{-1}}$. In figure 15 we clearly see a pattern, inherited from the incident wave, with higher horizontal velocities in the upper region of the wave front than those at the toe. This implies that the front is still steepening. Since the maximum inclination of the surface at $t = 3.05$ s is virtually vertical, this means that the wave front soon becomes

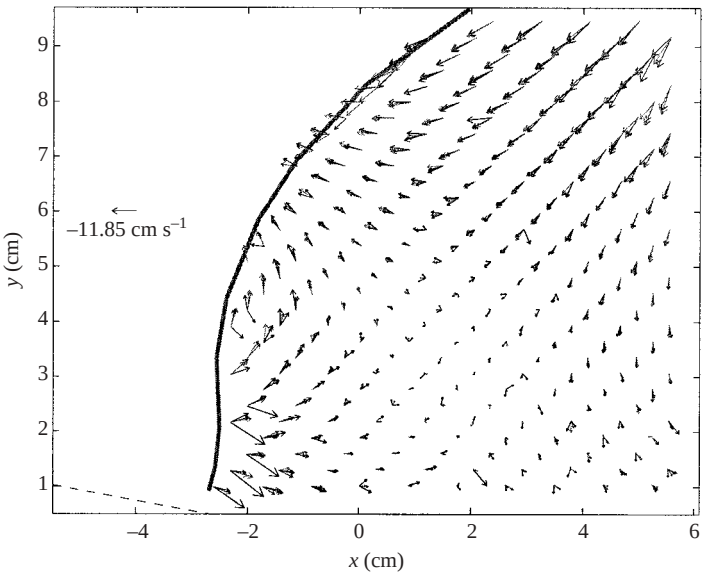

FIGURE 15. 'Deforming' velocity, $\boldsymbol{v}_d$ ($u_0 = 125\,\mathrm{cm\,s^{-1}}$) at $t = 3.05\,\mathrm{s}$ for case IV. The different arrows correspond to different repetitions of the experiments.

overturning. However, no clear signs of breaking are visible in video recordings or subsequent PIV images. This is due to the acceleration distribution. Accelerations are computed from the PIV velocities by a pseudo-tracing technique, as explained in § 2.2, and displayed in figure 14(*b*). Certainly, the accelerations are (at least) as sensitive to experimental scatter as $\boldsymbol{v}_d$. However, even though there are significant errors and no accelerations are measured in the vicinity of the fluid surface, we clearly observe a distinct pattern with large (compared to g), mainly horizontal, accelerations behind the toe, while the accelerations close to the top of the run-up front are much smaller, and with a strong downward component. This picture is very different from that of a breaking wave in deep water (New, McIver & Peregrine 1985). Clearly, the run-up acceleration pattern in figure 14(*b*) opposes the development of breaking and indicates a tendency toward thinning of the fluid front. Consequently, at the slightly later time $t = 3.12\,\mathrm{s}$ (figure 16) the overall picture of the flow has changed: we observe the embryo of an on-shore jet (see the introduction) with a clear stretching of the fluid tongue according to $\boldsymbol{v}_d$. The evolution of this early stage in the run-up is rapid, due to large accelerations possessing strong gradients. This bears a resemblance to features of wave impact on vertical walls, where a flip-through may lead to vertical jet up the wall (Cooker & Peregrine 1992). However, it must be noted that that paper reports accelerations that are an order of magnitude greater than those we have captured in the experiments. The occurrence of breaking during run-up is then determined by the competition between two features, namely the velocity distribution conveyed from the incident wave, which points to breaking, and the opposing acceleration field.

A few additional comments should be made on the run-up of a nearly breaking wave. First we have the analogy to the classical dam-break problem (Stoker 1957). To make this link clearer we introduce a coordinate system with axes parallel and normal to the beach plane. Moreover, at a time when the fluid front is nearly vertical, we choose the initial velocity of the system equal to the particle velocity at

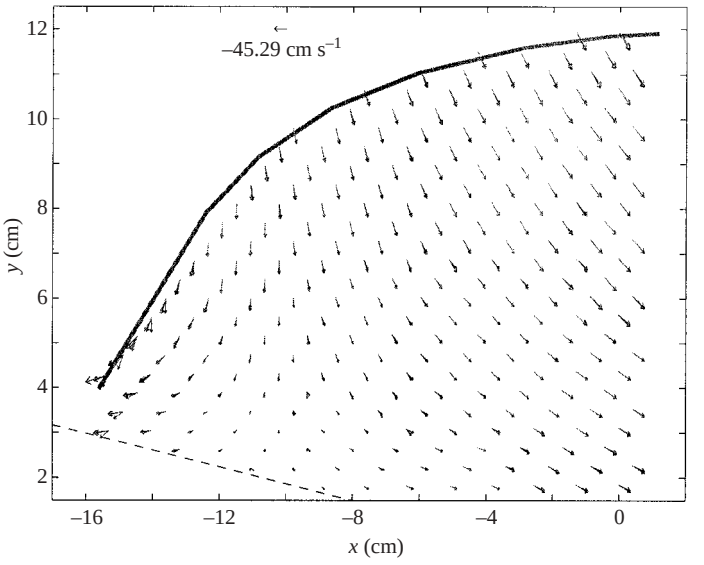

FIGURE 16. $\boldsymbol{v}_d$ ($u_0 = 170\,\mathrm{cm\,s^{-1}}$) at $t = 3.12\,\mathrm{s}$ for case IV.

the instantaneous shoreline, while the acceleration of the system is specified as the component of gravity parallel to the slope. We then arrive at a formulation of an initial value problem with a steep fluid front, nearly at rest, and an external force field (gravity + fictitious) normal to the bottom. The remaining difference from the standard dam-break problem is the presence of velocities behind the front, which presumably are not crucial. In the shallow-water context Peregrine & Williams (2001) report the connection between swash from incident bores and dam-break, including some consideration of velocities behind the bore front. For an ideal fluid the dam-break problem yields large accelerations at the bottom of the fluid front. If the contact angle between fluid and bottom is 90°, or larger, we obtain a singularity. The qualitative agreement with the accelerations in figure 14(*b*) is striking (see figure 19 in the Appendix). Naturally, the presence of the thin viscous boundary layer in the experiments prevents too extreme accelerations. We are not able, in any case, to measure very close to the fluid boundary. The dam-break analogy is elaborated further in the Appendix.

From the acceleration measurements we may also infer that a long-wave approximation, even a higher-order one, is not likely to be valid at this stage in run-up, when the on-shore jet is initiated. This is seen from the large vertical accelerations in figure 14(*b*) as well as the profiles in figure 17, which are both irreconcilable with long-wave theory. This is consistent with the analysis of the Appendix with respect to the dam-break problem in a long-wave context.

The somewhat gentler case II resembles case IV. In the run-up zone the wave is slightly less steep, but the quantitative patterns for the velocities and accelerations are similar, with a transition to a stretching velocity field and formation of a jet (results not shown).

For case IV the Boussinesq solution breaks close to $t = 3.05\,\mathrm{s}$. However, we observe fair agreement between computed velocities at the slightly earlier time $t = 3.045\,\mathrm{s}$ and experiments. Horizontal velocity profiles are shown in figure 17.

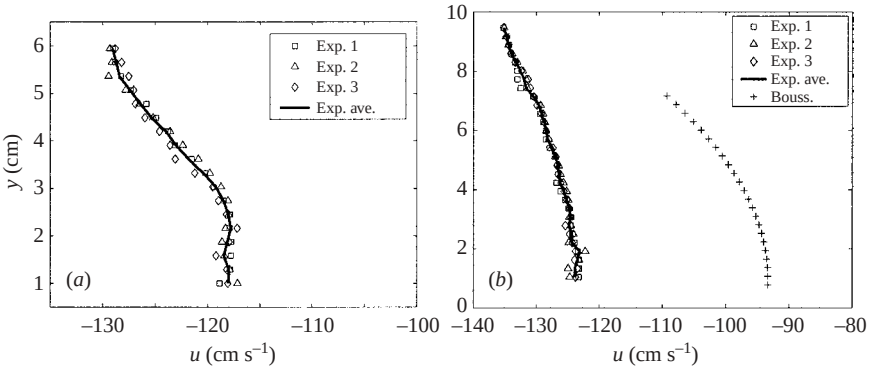

FIGURE 17. Case IV, $t_{tr} = 3.05\,\mathrm{s}$: Velocity profiles of u. (*a*) $x = -1.4\,\mathrm{cm}$, beyond the wave front of the Boussinesq solution. (*b*) $x = 4.0\,\mathrm{cm}$. Boussinesq results for $t = 3.045\,\mathrm{s}$ are included.

Case	A/h	A/h	R/A (B.)	R/A (Syn.)	R/A	R/A
I	0.12	—	3.7	3.9	3.7	—
II	0.53	—	**	**	3.3	—
III	0.335	0.34^{+}	4.1	**	3.5	3.1
IV	0.655	0.62	**	**	3.1	3.1
h (cm)	20	10	—	—	20	10

TABLE 4. Run-up height; B. – Boussinesq simulations and Syn. – analytic result derived from (2.9). The values marked by ** are dubious or meaningless due to wave breaking in the applied model. $^{+}$: the amplitude for case III and $h = 10\,\mathrm{cm}$ is uncertain and probably a little too high (§ 3.1), but the scaling effect in R/A is still significant.

4.4. *Run-up observations*

We have also measured the run-up heights by direct eye observation. With regard to scaling effects, we have also measured run-up for cases III and IV in the scaled-down experiments with $h = 10\,\mathrm{cm}$. For the steeper incident waves of cases II and IV, there were marked lateral variations of the front of the experimental run-up tongue when this approached the maximum elevation. As stated in § 2.1 this may be mainly due to a tiny curvature in the profile of the upper part of the beach. Preliminary tests with another beach, carefully constructed to avoid this problem, indicate that this is the case. The subjectivity of the method employed, combined with the slightly ambiguous definition of the fluid front for cases II and IV, points to significant errors. However, the results were repeatable within about a cm. The observations are summarized in table 4, together with theoretical values. One result that may seem surprising is the the apparent, though gentle, decrease of the ratio R/A (run-up height to amplitude of incident waves) with A/h, unlike the long-wave theory that predicts an increase in R/A with A/h. This may partly be due to viscosity and capillary effects, which are important on the laboratory scale, particularly in the thin upper part of the run-up tongue. Experiments by Langsholt (1981), reviewed in Pedersen & Gjevik (1983), showed a scaling effect for solitary wave run-up on a plane with $\theta = 10^{\circ}$, in the sense that R/A increased markedly with h for constant A/h. It should be noted that these experimental data did not systematically include amplitudes as high as cases II and

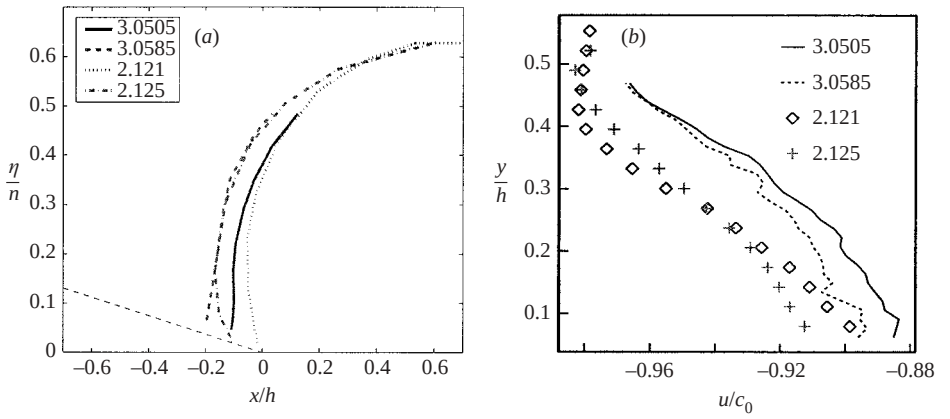

FIGURE 18. Case IV, $t_{tr} \approx 3.05$ s ($h = 20$ cm) and $t_{tr} \approx 2.12$ s ($h = 10$ cm) for two different times. (*a*) Surface profiles. (*b*) Velocities. The upper region of nearly constant u, observed for $t_{tr} = 2.121$ s is due to experimental errors near the surface. The remainder of this profile, as well as almost the whole profile for $t_{tr} = 2.125$ s, is measured accurately with good repeatability.

IV. In accordance with Langsholt we find a marked decrease in R/A for case III when h is reduced to 10 cm. The absolute run-up lengths are longer for case IV, which presumably should give more pronounced effects of friction. In spite of this, we obtain the same value $R/A = 3.1$ in both depths, which at first sight suggests that there is no scaling effect for case IV. However, that such an effect probably is present can be inferred from the amplitudes in finite depth. According to § 3.2, A/h of case IV is reduced from 0.66 to 0.62 when the depth is halved. If we interpolate between the results of cases II and IV, we find that $A/h = 0.62$ would give an R/A slightly above 3.2 for $h = 20$ cm. However, it is noteworthy that the scaling effect is that small for the higher amplitudes. The explanation is probably to be found in the thickness and other characteristics of the run-up tongue. Unfortunately, we have no measurements of these features at present.

We find good agreement between the long-wave theories and experiments for the gentle wave of case I, where the viscous effects should also be small since the run-up tongue is comparatively thick and short. It may be argued that (2.9) is not relevant for case I since the incident wave deviates significantly from a perfect solitary wave. But, the Boussinesq model yields $R/A = 3.69$ for an incident solitary wave, completely consistent with (2.5), which implies that case I yields the same maximum run-up as a solitary wave of the same height and that (2.9) does apply. According to equation (2.7) the analytical result (2.9) is meaningful only for case I, since the theory behind it predicts breaking for cases II to IV. Naturally, the Boussinesq model has a somewhat wider range of validity, but overestimates the run-up for case III substantially. For case III we observe a significant scale dependence, which points to a reduced error at a larger scale, as in an actual swell or tsunami situation. For cases II and IV the maximum run-up from the Boussinesq model is conceptually dubious (see § 2.6).

4.5. *Scaling effects*

Scaling effects on the beach were also checked for case IV. Surface profiles and horizontal velocities were extracted from the experiments with depth $h = 20$ cm and compared with $h = 10$ cm. Figure 18(*a*) shows some minor deviations in the surface profile at the 'toe' of the wave, possibly an indication of a boundary layer effect.

The difference in the horizontal position is not large, $\Delta x/h \approx 0.07$, and might be caused, partly, by the accuracy of the triggering. Figure 18(*b*) shows a difference in the velocities of about 4%.

5. Conclusion

Our investigation is mainly devoted to the phase of run-up where the wave fronts are at their steepest, namely the vicinity of the equilibrium shoreline. Utilizing the PIV technique, we have obtained good velocity measurements with a high degree of repeatability. Accelerations, on the other hand, have been obtained only under favourable conditions, and then with limited accuracy. Nevertheless, important information is present in the acceleration fields that have been found.

For a gentle incident wave, with $A/h = 0.12$, we found close agreement with the Boussinesq model, though there are minor discrepancies. The incident solitary wave with amplitude $A/h = 0.34$ becomes rather steep during run-up, but is yet far from breaking. The Boussinesq model still performs quite well, but the differences with the experiments are much more pronounced than for the previous case. The generated solitary wave has excess width due to over-representation of dispersion in the model. Moreover, its evolution early in the run-up is too rapid.

Close to the equilibrium shoreline, the highest incident wave ($A/h = 0.66$) becomes a body of water with a very steep head. This moves with a high and nearly uniform celerity, but the velocity variations can still be extracted from the PIV measurements. At a moment when the surface is almost vertical the velocity distribution still implies further steepening, which means that the wave becomes 'overhanging'. This is in fact observed directly in complementary measurements with $h = 10$ cm (see figure 18). However, the steepening deformation pattern is swiftly reversed through a transformation of the velocity distribution to a stretched one, pointing to the generation of a smooth run-up tongue. Calculation of accelerations from the PIV velocities reveals a pattern consistent with the rapid qualitative change of the velocity field. The acceleration pattern is qualitatively very similar to the dam-break problem. Like the dam-break problem large accelerations are present near the contact point between the surface and bottom, but we have so far not been able to resolve this region accurately in the PIV measurements. It is clear that vertical structures are important for the generation of the run-up tongue from the collapse of the steep wave front. Moreover, presuming that the collapse of a bore may have similar features, this casts doubt on the applicability of depth-averaged descriptions for bore run-up. However, further investigations are needed to establish any general conclusion on modelling of breaking waves. Such studies should involve extensive model testing as well as measurements on a wider spectrum of incident waves, preferably including fully developed bores. Improved experimental practice, enabling resolution of boundary layer, run-up tongues and turbulence is also desirable.

Measurements of maximum run-up heights is a secondary issue in the present investigation. Both the Boussinesq model and the analytical shallow-water result from Synolakis (1987) are good for the incident wave with $A/h = 0.12$. For the higher incident waves the long-wave theories overestimate the maximum run-up substantially. Moreover, unlike the theories, the experiments display a slight decrease in R/A with A/h, even though none of the waves are breaking. To some extent both this trend and the discrepancies with the theories may be attributed to viscous and capillary effects. However, that R/A for the highest wave displays very little change when h is reduced from 20 cm to 10 cm suggests that this is not the full explanation.

Most likely, there is a parameter range with nearly constant or reduced R/A as a function of A/h between the long-wave and breaking regimes. Moreover, the existence of this, as well as the lack of scaling effects, should probably be understood through the transition between the wave front and the swash. Unfortunately, at present we have insufficient data to support a firm conclusion.

This work was conducted under the Strategic University Programme 'General Analysis of Realistic Ocean Waves' funded by the Research Council of Norway. Discussions with J. Kristian Sveen, Didier Clamond and John Grue, and the technical assistance by Arve Kvalheim and Svein Vesterby are gratefully acknowledged.

Appendix. The dam-break problem

In the dam-break problem a body of water on a flat bed is released from rest under the action of gravity. Most attention has been given to the case with a semi-infinite fluid shelf with a vertical front. At the first instant a potential flow solution of the problem, yielding pressures and accelerations, is readily obtained by Fourier series. At the toe of the fluid front the potential solution displays a singularity, giving infinite values for the acceleration. The presence of this feature is easily inferred from the structure of the boundary value problem. At the free surface the pressure is zero, while the normal derivative at the bottom must counterbalance gravity to give zero vertical acceleration. At a contact point between the free surface and the bottom this implies large horizontal gradients for contact angles close to 90°, whereas perpendicular contact leads to a double-valued vertical derivative and singularity. For large times there exist asymptotic shallow-water solutions for the evolution of the fluid front. The key point is that the front rapidly evolves into a thin tongue with no bore-like features. This kind of dam-break problem is reviewed in Stoker (1957), while a fresh experimental and theoretical investigation is reported in Stansby, Chegini & Barnes (1998). Other initial shapes have also been investigated, with relevance to, for instance, the collapse of fluid columns produced by underwater explosions.

A simple initial shape, not very different from the wave front in the early stages of run-up, is a semicircle. Again discrete Fourier series can be applied for the initial pressure distribution. Details are given in Martin *et al.* (1952), which also contains numerical solutions for larger times, still based on Fourier series. For the acceleration at the free surface Martin *et al.* (1952) reported the closed-form expression

$$a_r = -\frac{2g}{\pi}\left(1 + \cos\theta \ln\left(\tan\frac{\theta}{2}\right)\right), \tag{A 1}$$

where θ is the angle between the radii and the positive horizontal axis. We note that a_r is scaled only by g and that the tangential acceleration equals the tangential component of gravity. The acceleration distribution in the interior is given by a Fourier series that converges except at the contact points. The result is displayed in figure 19. In spite of the differences with respect to surface shape etc. the similarity with the measured accelerations in figure 14(*b*) is striking.

Naturally, the Boussinesq equations are not likely to reproduce the circular dam-break accurately. However, in view of the relations between these problems and run-up, it would be instructive to observe how long-wave theory fails. In fact, generalized dam-break problems, including cases with contact angles less than 90° would probably serve as excellent benchmark problems for the applicability of simplified theories in general. Assuming a horizontal bottom and zero velocities, the Boussinesq equations

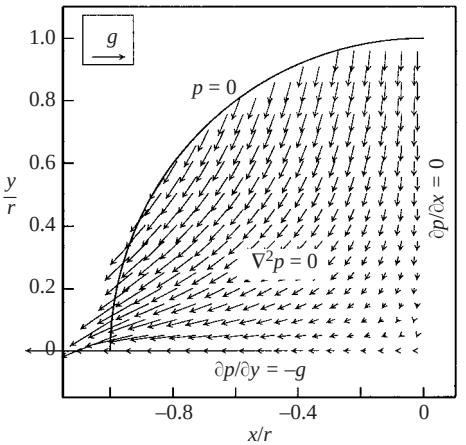

FIGURE 19. Accelerations from the 'circular' dam-break problem. The size of the reference arrow corresponds to the constant of gravity. The definition of the dam-break boundary value problem, formulated in terms of the pressure, is also indicated in the figure.

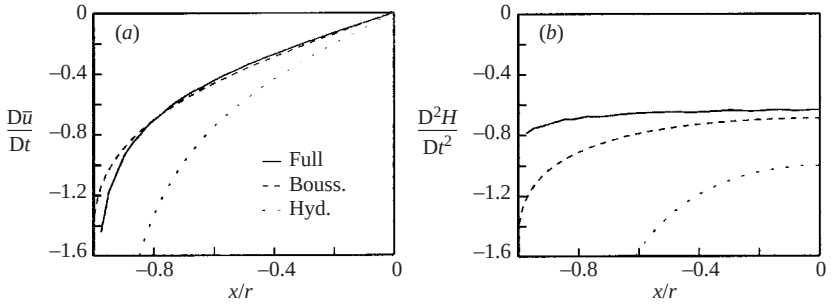

FIGURE 20. Comparison of full potential theory and long-wave equations for the circular dam-break problem. The accelerations are scaled by gravity.

(2.5) simplify and we may readily obtain second-order ordinary differential equation for either $\mathrm{D}\overline{u}/\mathrm{D}t$ or $\mathrm{D}^2H/\mathrm{D}t^2$ at $t = 0$:

$$\frac{\mathrm{D}\overline{u}}{\mathrm{D}t} - \frac{\beta}{3H}\frac{\mathrm{d}}{\mathrm{d}x}\left(H^3\frac{\mathrm{d}}{\mathrm{d}x}\frac{\mathrm{D}\overline{u}}{\mathrm{D}t}\right) = -\frac{\mathrm{d}H}{\mathrm{d}x}, \tag{A 2}$$

$$\frac{\mathrm{D}^2H}{\mathrm{D}t^2} - \frac{\beta}{3H}\frac{\mathrm{d}}{\mathrm{d}x}\left[\frac{1}{H}\frac{\mathrm{d}}{\mathrm{d}x}\left(H^2\frac{\mathrm{D}^2H}{\mathrm{D}t^2}\right)\right] = H\frac{\mathrm{d}^2H}{\mathrm{d}x^2}, \tag{A 3}$$

where the scaling is as in § 2.3. We observe that the left-hand operators become regularly singular when H has a zero of order 1 or $\frac{1}{2}$. When the contact angle is $\frac{1}{2}\pi$, as for a semicircle, the right-hand sides are also singular. In the hydrostatic case this singularity is conveyed directly to the solutions and we obtain singularities that are much stronger than for full potential theory as defined in figure 19. When the dispersive terms are retained, on the other hand, the singularity vanishes and the acceleration becomes finite at the contact points (we have local expansions like $\mathrm{D}\overline{u}/\mathrm{D}t = \kappa_0 + \kappa_{1/2}(x - x_c)^{1/2} + \cdots$, where x_c is the position of the contact point). Even though the absence of a singularity is in accordance with the physics, it must be regarded as a shortcoming of the Boussinesq theory. For the run-up simulations

the boundary condition at the fluid tip was $H = 0$. This is not consistent with the behaviour of $\mathrm{D}^2H/\mathrm{D}t^2$ as given by (A 3). However, in numerical solutions of the equations we obtain convergence, when refining the grid, toward a unique solution, regardless of the boundary condition mismatch. The solutions are displayed in figure 20 together with the corresponding quantities from the full potential flow solution. Apart from the neighbourhood of the contact point the Boussinesq solution displays very good accuracy for $\mathrm{D}\overline{u}/\mathrm{D}t$. The agreement for $\mathrm{D}^2H/\mathrm{D}t^2$ is not quite as good, indicating that Boussinesq theory is challenged not only by the steep gradients at the contact point, but also by the small overall length-to-depth ratio of the fluid body. Nevertheless the Boussinesq solution is much better than the hydrostatic one and they both predict large horizontal accelerations close to the fluid tip.

REFERENCES

Carrier, G. F. & Greenspan, H. P. 1958 Water waves of finite amplitude on a sloping beach. *J. Fluid Mech.* **4**, 97–109.

Chang, K.-A. & Liu, P. L.-F. 1998 Velocity, acceleration and vorticity under a breaking wave. *Phys. Fluids* **10**, 327–329.

Chang, K.-A. & Liu, P. L.-F. 1999 Experimental investigation of turbulence generated by breaking waves in water of intermediate depth. *Phys. Fluids* **11**, 3390–3400.

Cooker, M. J. & Peregrine, D. H. 1992 Wave impact pressure and its effect upon bodies lying on the sea bed. *Coastal Engng* **18**, 205–229.

Craig, K. R. & Thieke, R. J. 1996 Application of a digital particle image velocimetry (DPIV) system to breaking waves in the surf zone. In *25th Intl Conf. on Coastal Engineering* (ed. B. Edge), pp. 602–615. ASCE.

Dabiri, D. & Gharib, M. 2001 Simultaneous free-surface deformation and near-surface velocity measurements. *Exps. Fluids* **30**, 381–390.

Elfrink, B. & Baldock, T. 2002 Hydrodynamics and sediment transport in the swash and zone: a review and perspectives. *Coastal Engng* **45**, 149–167.

Flather, R. A. & Heaps, N. S. 1975 Tidal computations for morecambe bay. *Geophys. J. R. Astron. Soc.* **42**, 489–517.

Foote, M. & Horn, D. 1999 Video measurements of swash zone hydrodynamics. *Geomorphology* **29**, 59–76.

Grilli, S. & Svendsen, I. A. 1990 Computation of nonlinear wave kinematics during propagation and run-up on a slope. In *Water Wave Kinematics*. NATO ASI Series E, vol. 78, pp. 387–412. Kluwer.

Grilli, S., Svendsen, I. & Subramanya, R. 1997 Breaking criterion and characteristics for solitary waves on slopes. *J. Waterway, Port, Coastal Ocean Engrg* **123** (3), 102–112.

Guignard, S., Marcer, R., Rey, V., Kharif, K. & Fraunié, P. 2001 Solitary wave breaking on sloping beaches; 2-d two phase flow numerical simulation by sl-vof method. *Eur. J. Mech.* B/*Fluids* **20**, 57–74.

Hibberd, S. & Peregrine, D. H. 1979 Surf and run-up on a beach: a uniform bore. *J. Fluid Mech.* **95**, 323–345.

Jakobsen, M. L., Dewhirst, T. P. & Greated, C. A. 1997 Particle image velocimetry for predictions of acceleration fields and force within fluid flows. *Meas. Sci. Technol.* **8**, 1502–1516.

Jensen, A. & Grue, J. 2002 A note on the difference in the speed of gravity waves in a physical and numerical wave tank. *Wave Motion* **36**, 41–48.

Jensen, A., Sveen, J. K., Grue, J., Richon, J.-B. & Gray, C. 2001 Accelerations in water waves by extended particle image velocimetry. *Exps. Fluids* **30**, 500–510.

Johnsgard, H. 1999 A numerical model for run-up of breaking waves. *Intl J. Numer. Meth. Fluids* **31**, 1321–1331.

Johnsgard, H. & Pedersen, G. 1997 A numerical model for three-dimensional run-up. *Intl J. Numer. Meth. Fluids* **24**, 913–931.

Keller, H. B., Levine, A. D. & Whitham, G. B. 1960 Motion of a bore over a sloping beach. *J. Fluid Mech.* **7**, 302–316.

Keulegan, G. H. 1948 Gradual damping of solitary waves. *J. Res. Natl Bur. Stand.* **40**, 497–498.

Kowalik, Z. & Murty, T. S. 1993 Numerical simulation of two-dimensional tsunami run-up. *Marine Geodesy* **16**, 87–100.

Langsholt, M. 1981 Experimental study of wave run-up. Cand. real. thesis. Dept. of Mathematics, University of Oslo.

Li, Y. & Raichlen, F. 2001 Solitary wave runup on plane slopes. *J. Waterway, Port, Coastal Ocean Engrg* **127** (1), 33–44.

Lin, P., Chang, K.-A. & Liu, P. L.-F. 1999 Runup and rundown of solitary waves on sloping beaches. *J. Waterway, Port, Coastal Ocean Engng* **125** (5), 247–255.

Lin, P. & Liu, P. L.-F. 1998*a* A numerical study of breaking waves in the surf zone. *J. Fluid Mech.* **359**, 239–264.

Lin, P. & Liu, P. L.-F. 1998*b* Turbulence transport, vorticity dynamics, and solute mixing under plunging breaking waves in surf zone. *J. Geophys. Res.* **103**, 15677–15694.

Longo, S., Petti, M. & Losada, I. J. 2002 Turbulence in the swash and surf zones: a review. *Coastal Engng* **45**, 129–147.

Martin, J. C., Moyce, W. J., Penney, W. G., Price, A. T. & Thornhill, C. K. 1952 Some gravity wave problems in the motion of perfect liquids. *Phil. Trans. R. Soc. Lond.* A **244**, 231–334.

Meyer, R. E. & Taylor, A. D. 1972 Run-up on beaches. In *Waves on Beaches and Resulting Sediment Transport*. (ed. R. E. Meyer), pp. 357–411. Academic.

Nadoaka, K., Hino, M. & Koyano, Y. 1989 Structure of the turbulent flow field under breaking waves in the surf zone. *J. Fluid Mech.* **204**, 359–387.

New, A. L., McIver, P. & Peregrine, D. H. 1985 Computations of overturning waves. *J. Fluid Mech.* **150**, 233–251.

Pedersen, G. & Gjevik, B. 1983 Run-up of solitary waves. *J. Fluid Mech.* **135**, 283–299 (referred to herein as PG).

Peregrine, D. H. & Williams, S. M. 2001 Swash overtopping a truncated plane beach. *J. Fluid Mech.* **440**, 391–399.

Petti, M. & Longo, S. 2001 Turbulence experiments in the swash zone. *Coastal Engng* **43**, 1–24.

Puleo, J. A., Beach, R. A., Holman, R. A. & Allen, J. S. 2000 Swash zone sediment suspension and transport and the importance of bore-generated turbulence. *J. Geophys. Res.* **105** (C7), 17021–17044.

Raffel, M., Willert, C. E. & Kompenhans, J. 1998 *Particle Image Velocimetry, A Practical Guide*, 1st edn. Springer.

Shen, M. C. & Meyer, R. E. 1963 Climb of a bore on a beach. Part 3. Run-up. *J. Fluid Mech.* **16**, 113–125.

Shuto, N. 1976 Transformation of nonlinear long waves. *Coastal Engng* pp. 423–440.

Stansby, P. K., Chegini, A. & Barnes, T. C. D. 1998 The initial stages of dam-break flow. *J. Fluid Mech.* **374**, 407–424.

Stoker, J. 1957 *Water Waves*. Interscience.

Synolakis, C. E. 1987 The run-up of solitary waves. *J. Fluid Mech.* **185**, 523–545.

Synolakis, C. E. 1990 Generation of long waves in the laboratory. *J. Waterway, Port, Coastal, Ocean Engng* **116** (2), 252–266.

Synolakis, C. E. & Skjelbreia, J. E. 1993 Evolution of maximum amplitude of solitary waves on plane beaches. *J. Waterway, Port, Coastal, Ocean Engng* **119** (3), 323–342.

Tanaka, M. 1986 The stability of solitary waves. *Phys. Fluids* **29**, 650–655.

Ting, F. C. K. & Kirby, J. T. 1995 Dynamics of surf-zone turbulence in a strong plunging breaker. *Coastal Engng* **24**, 177–204.

Ting, F. C. K. & Kirby, J. T. 1996 Dynamics of surf-zone turbulence in a spilling breaker. *Coastal Engng* **27**, 131–160.

Titov, V. V. & Synolakis, C. E. 1998 Numerical modeling of tidal wave runup. *J. Waterway, Port, Coastal, Ocean Engng* **124** (4), 157–171.

Wood, D., Pedersen, G. & Jensen, A. 2003 Modeling of run-up of steep non-breaking waves. *Ocean Engng* **30**, 625–644.

Zelt, J. & Raichlen, F. 1990 A Lagrangian model for wave-induced harbour oscillations. *J. Fluid Mech.* **213**, 203–225.